J. Fluid Mech. (2000), *vol.* 417, *pp.* 103–126. Printed in the United Kingdom

New results in rotating Hagen–Poiseuille flow

By D. R. BARNES AND R. R. KERSWELL

Department of Mathematics, University of Bristol, Bristol, BS8 1TW, UK
email: R.R.Kerswell@bris.ac.uk

(Received 22 November 1999 and in revised form 1 March 2000)

New three-dimensional finite-amplitude travelling-wave solutions are found in rotating Hagen–Poiseuille flow (RHPF[Ω_a, Ω_p]) where fluid is driven by a constant pressure gradient along a pipe rotating axially at rate Ω_a and at Ω_p about a perpendicular diameter. For purely axial rotation (RHPF[$\Omega_a, 0$]), the two-dimensional helical waves found by Toplosky & Akylas (1988) are found to become unstable to three-dimensional travelling waves in a supercritical Hopf bifurcation. The addition of a perpendicular rotation at low axial rotation rates is found only to stabilize the system. In the absence of axial rotation, the two-dimensional steady flow solution in RHPF[$0, \Omega_p$] which connects smoothly to Hagen–Poiseuille flow as $\Omega_p \to 0$ is found to be stable at all Reynolds numbers below 10^4. At high axial rotation rates, the superposition of a perpendicular rotation produces a 'precessional' instability which here is found to be a supercritical Hopf bifurcation leading directly to three-dimensional travelling waves. Owing to the supercritical nature of this primary bifurcation and the secondary bifurcation found in RHPF[$\Omega_a, 0$], no opportunity therefore exists to continue these three-dimensional finite-amplitude solutions in RHPF back to Hagen–Poiseuille flow. This then contrasts with the situation in narrow-gap Taylor–Couette flow where just such a connection exists to plane Couette flow.

1. Introduction

All experimental and numerical evidence to date points to the fact that the transition to turbulence in unidirectional shear flows originates with a finite-amplitude instability of the laminar flow. The exact point of bifurcation beyond a minimum Reynolds number Re_t depends sensitively on the initial conditions and appears to lead directly to a high-dimensional state of some spatial and temporal complexity (Reynolds 1883; and e.g. Darbyshire & Mullin 1995; Draad, Kuiken & Nieuwstadt 1998 and references therein for pipe flow). One approach to understanding the numerical value of this threshold Reynolds number has been to identify the Reynolds number Re_g at which the laminar state is no longer a global attractor. This coincides with the birth of new limit sets in phase space (solutions to the Navier–Stokes equations) which appear a necessary precursor to support the complex dynamics observed after transition. The issue is then whether Re_g is a useful predictor for the observed minimum transitional Reynolds number Re_t.

Energy stability arguments (Serrin 1959; Joseph 1976) furnish a rigorous lower bound Re_e on Re_g but this is known to be very conservative for shear flow problems. Alternatively, an upper bound follows immediately once the existence of any non-trivial solution is established at a given Reynolds number. This has motivated a direct attack on finding new fixed points (steady solutions) or periodic states (travelling-wave solutions) to the full dynamical system of shear flow (the Navier–Stokes equations

with appropriate forcing and boundary conditions). In practice, these new solutions can only realistically be found through continuation methods since the basic tool (Newton's method) fails to converge unless given a very good initial guess at the fixed point. In plane Poiseuille flow (PPF), the Hopf bifurcation point at $Re = 5772$ on the laminar flow (Orszag 1971) has been used as a starting point to trace two-dimensional travelling waves back to $Re \approx 2900$ (Zahn *et al.* 1974; Herbert 1977) and then three-dimensional travelling waves back to $Re \approx 1000$ (Ehrenstein & Koch 1991). This is close to measured transitional values (Davies & White 1928; Patel & Head 1969; Carlson, Widnall & Peeters 1982) (in contrast $Re_e = 49.6$ for PPF). Where a starting bifurcation point is not available, a standard trick is to embed the problem of interest within a larger family for which one does exist (homotopy). Solutions obtained through a known bifurcation sequence in one point of parameter space then offer possibilities for continuation back to the original problem of interest. Using just such an approach, Nagata (1990) was able to continue three-dimensional steady solutions in the narrow-gap Taylor–Couette problem back to plane Couette flow (PCF) for Reynolds numbers close to 125 (for more recent work see Cherhabili & Ehrenstein 1995, 1997; Nagata 1997, 1998). The presence of these saddle points in phase space (the solutions were found to be unstable by Clever & Busse 1992, 1997) indicates that $Re_e = 20.7 \leqslant Re_g \lesssim 125$ for PCF whereas experiments and numerics suggest $Re_t \approx 350$ (Lundbladh & Johansson 1991; Tillmark & Alfredsson 1992; Daviaud, Hegseth & Bergé 1992; Dauchot & Daviaud 1995). This difference is of considerable current interest (e.g. Schmiegel & Eckhardt 1997; Eckhardt & Mersmann 1999).

In contrast, no non-trivial solutions have been reported for the third canonical shear case, Hagen–Poiseuille flow (HPF) (Patera & Orszag 1981; Landman 1990*a*, *b*), despite some suggestive asymptotic analyses (Davey & Nguyen 1971, Smith & Bodonyi 1982). This gap motivates the present study in which, following the lead of Nagata (1990), we embed HPF within a two-parameter family of rotating Hagen–Poiseuille problems (RHPF$[\Omega_a, \Omega_p]$) where Ω_a represents the axial rotation rate and Ω_p the perpendicular rotation rate about a diameter. The existence of linear instability at low axial rotation rates in RHPF$[\Omega_a, 0]$ (Mackrodt 1976) justifies this embedding by providing a starting bifurcation point to possibly continue solutions back to HPF. The fact that the bifurcating flow has a relatively simple spatial structure is crucial in allowing progress with limited storage and finite processor speeds. A previous attempt at a 'geometrical' embedding – elliptic pipe flow – proved too numerically expensive to follow the spatially complex bifurcating flow (the aspect ratio of semi-major to semi-minor axis must be over 10 to find PPF-type linear instability, Kerswell & Davey 1996). We also take the opportunity to study the superposition of these rotations which, as formulated here, describes a precessing pipe. The pipe has an axial spin in a frame which itself is rotating about a perpendicular axis fixed in the laboratory. This means that the family RHPF$[\Omega_a, \Omega_p]$ encompasses flows which experience precessional 'shearing' instabilities (Kerswell 1993; Mahalov 1993) and therefore is assured to possess other candidate bifurcation points for continuation (albeit at 'fast' axial rotation rates).

The purpose of this paper is to investigate whether finite-amplitude solutions can be found in HPF through continuation of solutions identified in RHPF. The specific issues to be addressed in this investigation can be listed as follows.

(i) *Can finite-amplitude travelling-wave solutions in* RHPF$[\Omega_a, 0]$ *be continued back to* HPF? The Hopf bifurcation found by Mackrodt (1976) is known to be supercritical leading to two-dimensional helical travelling waves which therefore grow in amplitude

as Ω_a increases away from the HPF limit (Toplosky & Akylas 1988; Landman 1990*a*, *b*; Yang & Leibovich 1991). It remains an open question as to whether a branch of three-dimensional travelling waves may branch off from these helical waves in a secondary bifurcation and lead back to the HPF limit. This situation would then be completely analogous to the rotating PCF situation uncovered by Nagata (1990).

(ii) *Is the two-cell laminar flow in* RHPF$[0, \Omega_p]$ *linearly unstable for experimentally interesting Reynolds numbers of* $O(1000)$*?* Sharma & Nandakumar (1995) have shown that multiple steady two-dimensional flow solutions exist in RHPF$[0, \Omega_p]$. They confirmed the presence of a two-cell flow (Barua 1954; Benton 1956) which connects smoothly with HPF as $\Omega_p \to 0$ but also found a four-cell flow in some circumstances. The two-cell flow could be nonlinearly unstable (leading to the four-cell flow) but appeared linearly stable to two-dimensional disturbances over the limited parameter range studied. In this paper, we concentrate exclusively on this two-cell flow solution and re-examine its linear stability to fully three-dimensional disturbances with the intention of identifying alternative starting points for continuation back to HPF.

(iii) *How does the neutral curve in the* (Ω_a, Re) *plane of* RHPF$[\Omega_a, 0]$ (Pedley 1969; Mackrodt 1976) *extend as a surface into* (Ω_a, Ω_p, Re) *space?* In particular, does it connect with any neutral curve in the (Ω_p, Re) plane and how does it relate to the neutral curve known to exist in the (Ω_a, Ω_p) plane (Kerswell 1993; Mahalov 1993)?

2. Formulation

2.1. *Governing equations*

The HPF problem consists of an incompressible fluid of constant density ρ and kinematic viscosity ν flowing in a circular pipe of radius s_0 under the action of a constant applied pressure gradient

$$\nabla p^* = -\frac{4\rho\nu U}{s_0^2}\widehat{\boldsymbol{z}}. \tag{2.1}$$

At low enough values of the Reynolds number $Re = s_0 U/\nu$, the realized flow is uniquely

$$\boldsymbol{u}^* = U\left(1 - \frac{s^2}{s_0^2}\right)\widehat{\boldsymbol{z}}, \tag{2.2}$$

in the usual cylindrical polar coordinate system (s, ϕ, z). For RHPF, the pipe is further considered to be rotating with angular velocity $\Omega_a^*\widehat{\boldsymbol{z}}$ about its axis, which itself is rotating at $\Omega_p^*\widehat{\boldsymbol{x}}$ about a diameter (see figure 1). In a frame rotating at $\Omega_p^*\widehat{\boldsymbol{x}} = \Omega_p^*(\widehat{\boldsymbol{s}}\cos\phi - \widehat{\boldsymbol{\phi}}\sin\phi)$, the governing equations (non-dimensionalized using the centreline speed U and pipe radius s_0) for RHPF(Ω_a, Ω_p) are

$$\frac{\partial \boldsymbol{u}}{\partial t} + 2\Omega_p\widehat{\boldsymbol{x}} \times \boldsymbol{u} + \boldsymbol{u}\cdot\nabla\boldsymbol{u} + \nabla(p - \tfrac{1}{2}|\Omega_p\widehat{\boldsymbol{x}}\times\boldsymbol{r}|^2) = \frac{1}{Re}\nabla^2\boldsymbol{u}, \tag{2.3}$$

$$\nabla\cdot\boldsymbol{u} = 0, \tag{2.4}$$

with boundary condition $\boldsymbol{u} = \Omega_a\widehat{\boldsymbol{\phi}}$ at $s = 1$, where

$$\Omega_p = \frac{\Omega_p^* s_0}{U}, \quad \Omega_a = \frac{\Omega_a^* s_0}{U}, \quad \boldsymbol{u} = \frac{\boldsymbol{u}^*}{U}. \tag{2.5}$$

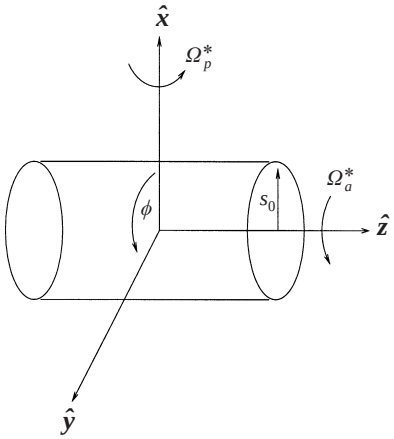

FIGURE 1. A diagram of the geometry and coordinate system under consideration.

Computationally, it is preferable to work with the 'perturbation' velocity and pressure fields, $\tilde{\boldsymbol{u}}$ and $\tilde{p}$, defined as follows

$$\boldsymbol{u} = (1-s^2)\widehat{\boldsymbol{z}} + \Omega_a s\widehat{\boldsymbol{\phi}} + \tilde{\boldsymbol{u}}(s,\phi,z,t), \tag{2.6}$$

$$p = -\frac{4z}{Re} + \tfrac{1}{2}|\Omega_p\widehat{\boldsymbol{x}}\times\boldsymbol{r}|^2 + \tfrac{1}{2}\Omega_a^2 s^2 + \tilde{p}(s,\phi,z,t), \tag{2.7}$$

which represent the deviation of the flow solution from the axially rotating extension of the HPF solution (2.2). In particular, $\tilde{\boldsymbol{u}}$ satisfies homogeneous boundary conditions and to fix the applied pressure gradient, $\tilde{p}$ is strictly periodic. The governing equations, (2.3) and (2.4), rewritten for these new variables,

$$\frac{\partial\tilde{\boldsymbol{u}}}{\partial t} + (2\Omega_p\widehat{\boldsymbol{x}} + \Omega_a\widehat{\boldsymbol{z}})\times\tilde{\boldsymbol{u}} + (1-s^2)\frac{\partial\tilde{\boldsymbol{u}}}{\partial z} + \Omega_a\frac{\partial\tilde{\boldsymbol{u}}}{\partial\phi} - 2s\tilde{u}\,\widehat{\boldsymbol{z}} + \tilde{\boldsymbol{u}}\cdot\nabla\tilde{\boldsymbol{u}}$$

$$+ \nabla\tilde{p} - \frac{1}{Re}\nabla^2\tilde{\boldsymbol{u}} = -2\Omega_p\widehat{\boldsymbol{x}}\times[(1-s^2)\widehat{\boldsymbol{z}} + \Omega_a s\widehat{\boldsymbol{\phi}}], \tag{2.8}$$

$$\nabla\cdot\tilde{\boldsymbol{u}} = 0, \tag{2.9}$$

make it clear that the trivial solution $(\tilde{\boldsymbol{u}},\tilde{p}) = (\boldsymbol{0},0)$ exists only if $\Omega_p = 0$. The extra Coriolis term present when $\Omega_p \neq 0$ induces a non-trivial secondary flow which has been the subject of many previous papers (Barua 1954; Benton 1956; Itō & Nanbu 1971; Duck 1983; Mansour 1985; Lei & Hsu 1990; Raszillier, Guiasu & Durst 1990; Sharma & Nandakumar 1995; Draad & Nieuwstadt 1998).

The rotational and reflectional symmetries of the RHPF(Ω_a,Ω_p) system mean that attention need only be focussed on positive rotations, $\Omega_a,\ \Omega_p \geqslant 0$. This is because an incompressible solution, $\tilde{\boldsymbol{u}} = (\tilde{u},\tilde{v},\tilde{w})(s,\phi,z,t)$ to RHPF(Ω_a,Ω_p), has counterparts $(\tilde{u},\tilde{v},\tilde{w})(s,\phi\pm\pi,z,t)$ in RHPF$(\Omega_a,-\Omega_p)$ and $(\tilde{u},-\tilde{v},\tilde{w})(s,-\phi,z,t)$ in RHPF$(-\Omega_a,-\Omega_p)$. A further trivial symmetry under the transformation $U\to -U$ means that we can confine attention entirely to the first quadrant in (Ω_a,Ω_p,Re) space.

2.2. *Numerics*

The problem, (2.8) and (2.9), was solved as stated, by 3 momentum + 1 continuity equations, in terms of the primitive variables $(\tilde{u},\tilde{v},\tilde{w},\tilde{p})$ rather than any reduced representation of the velocity field such as a poloidal–toroidal decomposition. Experience

indicates that this provides the best numerically conditioned formulation since spatial derivatives are kept at their lowest order. The governing equations were imposed by collocation over s and Galerkin projection over ϕ and z. The axis of the pipe can cause numerical problems unless specific efforts are made to desensitize the code to this artificial singularity. This was achieved here by exploiting the representation degeneracy of cylindrical polar coordinates in which the points $(-s, \phi \pm \pi, z)$ and (s, ϕ, z) are exactly equivalent. This means that each velocity component and scalar pressure function has a definite parity in s determined by whether its corresponding azimuthal wavenumber m is even or odd (see the appendix of Kerswell & Davey 1996). Building the appropriate radial parity into the spectral representation of each field variable not only saves on storage but automatically instils the correct limiting behaviour near the axis. Computationally, we consider the domain $\{-1 \leqslant s \leqslant 1, 0 \leqslant \phi < \pi\}$ rather than viewing the interior of the pipe as the region $\{0 \leqslant s \leqslant 1, -\pi \leqslant \phi < \pi\}$. The solution in $-1 \leqslant s < 0$ can be constructed from that in $0 < s \leqslant 1$ through the known symmetries and so we need only collocate the equations over the positive zeros of $T_{2N}(s)$ and impose boundary conditions at $s = 1$. Most importantly, this means that the collocation points are at their sparsest near the axis ($O(1/2N)$ spacing) and at their densest ($O(1/4N^2)$ spacing) near the sidewall where boundary layers typically need to be resolved.

We therefore look for travelling-wave solutions of the form

$$\begin{bmatrix} \tilde{u} \\ \tilde{v} \\ \tilde{w} \\ \tilde{p} \end{bmatrix} = \sum_{n=1}^{N} \sum_{l=-L}^{L} \left\{ \sum_{m=-M,\, m\,\mathrm{odd}}^{M} \begin{bmatrix} \tilde{u}_{lmn} \Theta_{2n}(s) \\ \tilde{v}_{lmn} \Theta_{2n}(s) \\ \tilde{w}_{lmn} \Theta_{2n+1}(s) \\ \tilde{p}_{lmn} T_{2n-1}(s) \end{bmatrix} \exp\left(\mathrm{i}m[\phi - c_\phi t] + l\alpha[z - c_z t]\right) \right.$$

$$\left. + \sum_{m=-M,\, m\,\mathrm{even}}^{M} \begin{bmatrix} \tilde{u}_{lmn} \Theta_{2n+1}(s) \\ \tilde{v}_{lmn} \Theta_{2n+1}(s) \\ \tilde{w}_{lmn} \Theta_{2n}(s) \\ \tilde{p}_{lmn} T_{2n-2}(s) \end{bmatrix} \exp\left(\mathrm{i}m[\phi - c_\phi t] + l\alpha[z - c_z t]\right) \right\}, \quad (2.10)$$

where α is the primary axial wavenumber, $T_n(s) = \cos(n \cos^{-1} s)$ is the nth Chebyshev polynomial and

$$\Theta_n(s) \equiv T_n(s) - T_{n-2}(s), \quad (2.11)$$

so that the boundary conditions are built into the spectral functions. Reality of the total velocity and pressure expansions enforces $\tilde{\boldsymbol{u}}_{-l-mn} = \tilde{\boldsymbol{u}}^*_{lmn}$ and $\tilde{p}_{-l-mn} = \tilde{p}^*_{lmn}$ (* meaning complex conjugation) so that only coefficients with $l \geqslant 0$ need be stored. This, together with the fact that $\tilde{u}_{00n} = \tilde{p}_{00n} = 0 \ \forall n$, means that there are $2N(4L(2M+1)+4M+1)$ real coefficients to be determined. Additionally, depending on the degree of phase degeneracy in the solution (helical waves have one degree and three-dimensional waves have two degrees), one or two of the phase conditions

$$\mathrm{Im}\left(\sum_{n=1}^{N} \tilde{u}_{1-1n} \Theta_{2n}(0)\right) = \mathrm{Im}\left(\sum_{n=1}^{N} \tilde{u}_{2-1n} \Theta_{2n}(0)\right) = 0 \quad (2.12)$$

are imposed. These equations act to determine the phase velocities, c_ϕ and c_z.

The resultant nonlinear algebraic system,

$$\mathscr{F}(\tilde{u}_{lmn}, \tilde{v}_{lmn}, \tilde{w}_{lmn}, \tilde{p}_{lmn}, c_\phi, c_z; Re, \Omega_a, \Omega_p, \alpha) = \mathbf{0}, \quad (2.13)$$

was solved given a nearby starting solution using the *PITCON* package developed by Rheinboldt & Burkardt (1983*a*, *b*) which is a robust branch-following program based

upon Newton–Raphson iteration. It was not practical to use more sophisticated branch-switching packages owing to the large number of equations to be solved in this study. Typical truncations used were $(N, M, L) = (9, 6, 6)$ (6068 and 6069 real equations, respectively) in § 3.1 and § 3.3, and $(N, M, L) = (12, 5, 5)$ (5786 real equations) in § 3.4 with storage requirements of $\approx$ 300 MBytes and convergence times (for the norm of the residual $\leqslant 10^{-12}$) of O(90–120) minutes on either a 300 MHz Ultrasparc or 195 Mhz R10 000 processor.

3. Results

3.1. *Three-dimensional travelling waves in* RHPF$[\Omega_a, 0]$

Mackrodt (1976) found that the first bifurcation in RHPF$(\Omega_a, 0)$ occurs at $\Omega_a \approx 27/Re$ through the mode $(m, l) = (-1, 1)$ with $\alpha \approx 106.6/Re$ in the limit $Re \to \infty$. The new branch of solutions corresponds to two-dimensional helical travelling waves of the form

$$\begin{bmatrix} \tilde{u} \\ \tilde{v} \\ \tilde{w} \\ \tilde{p} \end{bmatrix} = \sum_{n=1}^{N} \left\{ \sum_{m=-M,\, m\,\text{odd}}^{M} \begin{bmatrix} \tilde{u}_{mn}\Theta_{2n}(s) \\ \tilde{v}_{mn}\Theta_{2n}(s) \\ \tilde{w}_{mn}\Theta_{2n+1}(s) \\ \tilde{p}_{mn}T_{2n-1}(s) \end{bmatrix} \exp\left(\mathrm{i}m(\phi - c_\phi t - \alpha[z - c_z t]\right) \right.$$

$$\left. + \sum_{m=-M,\, m\,\text{even}}^{M} \begin{bmatrix} \tilde{u}_{mn}\Theta_{2n+1}(s) \\ \tilde{v}_{mn}\Theta_{2n+1}(s) \\ \tilde{w}_{mn}\Theta_{2n}(s) \\ \tilde{p}_{mn}T_{2n-2}(s) \end{bmatrix} \exp\left(\mathrm{i}m(\phi - c_\phi t - \alpha[z - c_z t]\right) \right\}, \quad (3.1)$$

where there is effectively one phase speed $c := c_z - c_\phi/\alpha$ directed along the pipe axis. Imposing the first of the two phase conditions given in (2.12) allowed this two-dimensional helical wave branch first found by Toplosky & Akylas (1988) to be traced out (in a frame translating at c along the axis). At $Re = 1000$, which is in the asymptotic $Re \to \infty$ regime, a truncation of $(N, M) = (9, 6)$ proves more than sufficient to capture the helical waves at rotation rates Ω_a an order of magnitude higher than the critical value, i.e. to $Re\Omega_a = O(300)$. (When capturing finite-amplitude solutions, sufficient accuracy will generally mean in this paper that the plotted quantity does not change visually with modified truncation levels. For stability calculations, sufficient accuracy will be convergence to at least 2 significant figures in the growth rates.)

The three-dimensional linear stability of these two-dimensional helical waves can be examined by superimposing a small disturbance of the form

$$\begin{bmatrix} \hat{u} \\ \hat{v} \\ \hat{w} \\ \hat{p} \end{bmatrix} = \exp\left(\mathrm{i}\mu\alpha z + \sigma t\right) \sum_{n=1}^{N} \left\{ \sum_{m=-M,\, m\,\text{odd}}^{M} \begin{bmatrix} \hat{u}_{lmn}\Theta_{2n}(s) \\ \hat{v}_{lmn}\Theta_{2n}(s) \\ \hat{w}_{lmn}\Theta_{2n+1}(s) \\ \hat{p}_{lmn}T_{2n-1}(s) \end{bmatrix} \exp\left(\mathrm{i}m(\phi - \alpha[z - ct]\right) \right.$$

$$\left. + \sum_{m=-M,\, m\,\text{even}}^{M} \begin{bmatrix} \hat{u}_{lmn}\Theta_{2n+1}(s) \\ \hat{v}_{lmn}\Theta_{2n+1}(s) \\ \hat{w}_{lmn}\Theta_{2n}(s) \\ \hat{p}_{lmn}T_{2n-2}(s) \end{bmatrix} \exp\left(\mathrm{i}m(\phi - \alpha[z - ct]\right) \right\}, \quad (3.2)$$

onto the helical waves and solving the subsequent two-dimensional eigenvalue problem for the eigenvalue $\sigma(\mu; \Omega_a, Re)$. Instability (at given Re and Ω_a) is assured if there exists a real value of the Floquet parameter μ such that $\sigma_r := \mathrm{Re}(\sigma) > 0$ (note the Floquet

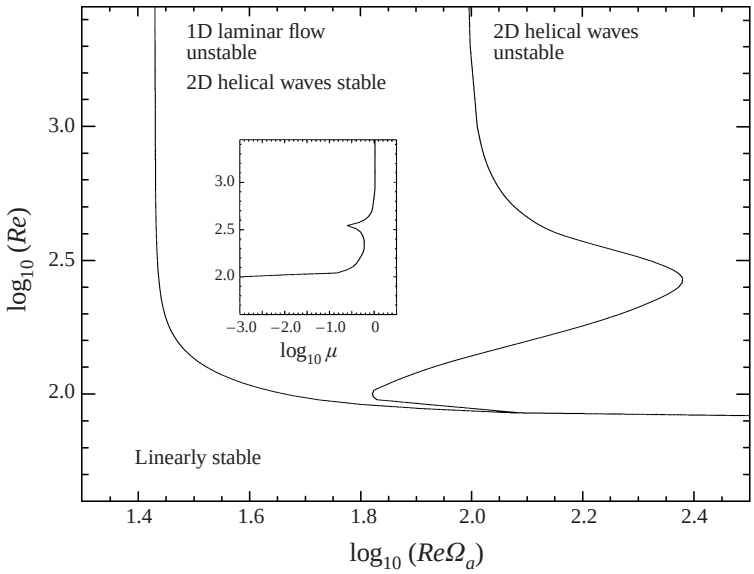

FIGURE 2. Secondary instability threshold for RHPF$[\Omega_a, 0]$. The curve shown is strictly an upper estimate on where the two-dimensional helical waves resulting from the primary bifurcation become unstable (upper estimate because only the limited Floquet parameter range $\mu \in (0, 4]$ is considered). The insert is a plot of $\log_{10}(Re)$ versus $\log_{10}\mu$ which shows how the critical μ value changes along the secondary stability boundary.

parameter for ϕ can be absorbed into the sum as the disturbance must be periodic in ϕ). Only the limited range $0 < \mu \leqslant 4$ was considered since it is only numerically practical to pursue fully three-dimensional travelling-wave solutions for small integer and simple fractional values of μ (negative values of μ need not be considered because $\sigma(-\mu) = \sigma^*(\mu)$). Figure 2 collects together the results of this stability analysis on Mackrodt's neutral-curve diagram. The instability boundary is strictly an upper estimate on where secondary instability of the primary two-dimensional helical waves occurs since only $\mu \in (0, 4]$ is considered.

Figure 2 shows that in the asymptotic limit of large Re ($\geqslant 1000$), $\mu \approx 1$ conveniently gives the minimum critical rotation rate. Three-dimensional travelling-wave solutions arising out of this bifurcation were then traced out for $\mu = 1$. Figure 3 indicates how the neutral eigenfunction is incorporated into the numerical truncation scheme. The new frequency, $\sigma_i := \mathrm{Im}(\sigma)$, introduced at this secondary Hopf bifurcation can be 'removed' by going into the appropriately moving frame translating at an axial velocity $c_z = -\sigma_i/(\alpha\mu)$ and rotating with angular velocity $c_\phi = \alpha(c_z - c)$. Figure 4 shows the bifurcation diagrams obtained at the three different Reynolds numbers of 100, 300 and 1000 for $\mu = 1$ (using a truncation of $(N, M, L) = (9, 6, 6)$). The secondary bifurcation is seen to be a supercritical Hopf bifurcation in which the new three-dimensional travelling-wave branch bends away from the HPF axis ($\Omega_a = 0$). Continuation even to relatively large rotation rates reveals that the solution branch does not turn back towards the zero rotation axis for any $200 \leqslant Re \leqslant 3000$. This then is in direct contrast to the situation in Taylor–Couette flow which Nagata (1990) was able to exploit. The $Re = 100$ curve is typical of the low-Reynolds-number situation (recall $Re_e = 81.49$, Joseph & Carmi 1969) in which the two-dimensional helical branch reconnects to the basic one-dimensional solution at higher rotation rates.

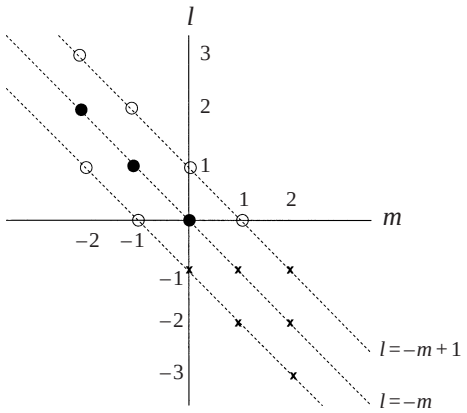

FIGURE 3. A schematic of how the fully three-dimensional travelling waves are captured. ●, The underlying helical wave solution; ○, the neutral eigenfunction at the bifurcation; ×, the modes that are implicitly included in the solution through the reality condition: only modes with $\ell \geqslant 0$ are stored. (For diagrammatic purposes, only the first few modes are shown.)

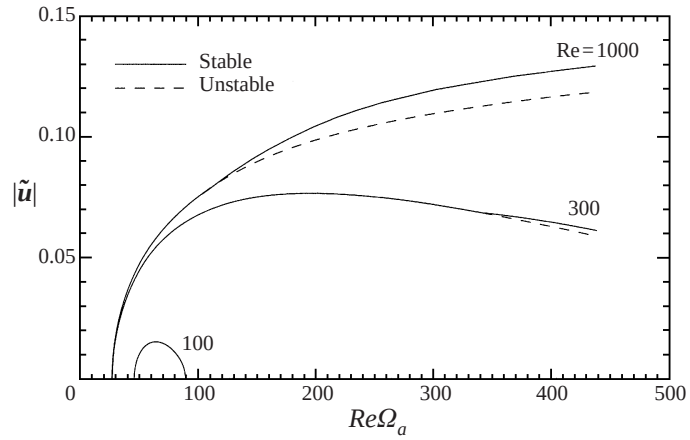

FIGURE 4. Bifurcation diagram showing the amplitude $|\tilde{\boldsymbol{u}}|$ of the disturbance against the rotational Reynolds number $Re\Omega_a$ for $(Re, \alpha) = (100, 0.71851), (300, 0.36777)$ and $(1000, 0.10695)$. Solid (dashed) lines represent stable (unstable) solutions as usual. At the secondary bifurcation point, the two-dimensional solution branch goes from being solid to dashed and the new solid line represents stable three-dimensional solutions.

This restabilization phenomenon has been noticed before by Conley (1996) in both rotating PCF and PPF. Figure 4 shows only that the two-dimensional helical branch at $Re = 100$ is stable to $\mu = 1$ disturbances: in fact, it loses stability at $Re\Omega_a = 66.225$ for $\mu = 0.001$.

The typical structure of the two-dimensional helical modes pre-instability is shown in figures 5(*a*) and 5(*b*). Two features stand out: the basic parabolic profile in the axial direction is noticeably flattened and the fluid significantly despun near the axis. Figures 5(*c*) and 5(*d*) compare the structure of the two-dimensional helical wave with the three-dimensional solution post-instability. Significantly, the now unstable two-dimensional solution has developed a mean axial flow with an off-axis maximum although this strictly occurs sometime after the loss of stability. For example, at

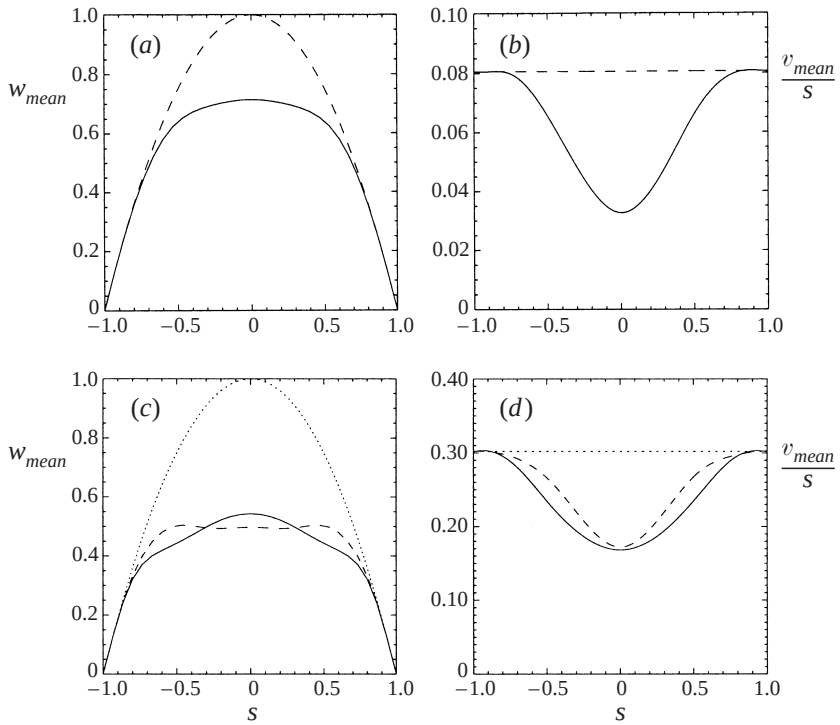

FIGURE 5. Structure of the two-dimensional helical solutions before the second bifurcation at $Re = 1000$, $\Omega_a = 0.0807$, $\alpha = 0.10695$; (*a*) axial mean flow, and (*b*) local angular velocity of the one-dimensional and two-dimensional solutions. The structure of the two-dimensional and three-dimensional solutions after the second bifurcation at $Re = 1000$, $\Omega_a = 0.302$, $\alpha = 0.10695$; (*c*) axial mean flow and (*d*) local angular velocity for one-dimensional, two-dimensional and three-dimensional solutions. (*a*, *b*) – – –, 1D base flow; ——, two-dimensional. (*c*, *d*) …, 1D base flow; – – –, two-dimensional; ——, three-dimensional.

$Re = 1000$ loss of stability occurs when $\Omega_a = 0.102$ whereas the off-axis maximum develops at $\Omega_a = 0.205$. In contrast, the preferred three-dimensional solution reverts back to a more parabolic-looking profile. Structurally, the three-dimensional solution has slightly less energy in the mean flow correction mode $(m, l) = (0, 0)$ whereas it houses more energy than the two-dimensional solution in the $(m, l) = (-1, 1)$ mode. Furthermore, the three-dimensionality is comparatively weak as there is only about 3% of the total three-dimensional solution energy off the two-dimensional 'diagonal' in (m, l) space.

The axial and azimuthal stresses exerted by these travelling-wave solutions on the pipe wall must vanish identically since the averaged angular and linear momenta of the waves are invariant as they propagate along and around the pipe. However, each wave will have a distinctive viscous dissipation rate D per unit length associated with it. The relevant power balance is

$$\mathrm{D} := \frac{1}{Re}\left(\iiint |\nabla \boldsymbol{u}|^2 \,\mathrm{d}V - \iint_{s=1} \frac{v^2}{s}\,\mathrm{d}\phi\,\mathrm{d}z\right) = -\iiint \boldsymbol{u}\cdot\nabla p\,\mathrm{d}V + \frac{1}{Re}\iint_{s=1} v\left[s\frac{\partial}{\partial s}\frac{v}{s}\right]\mathrm{d}\phi\,\mathrm{d}z, \quad (3.3)$$

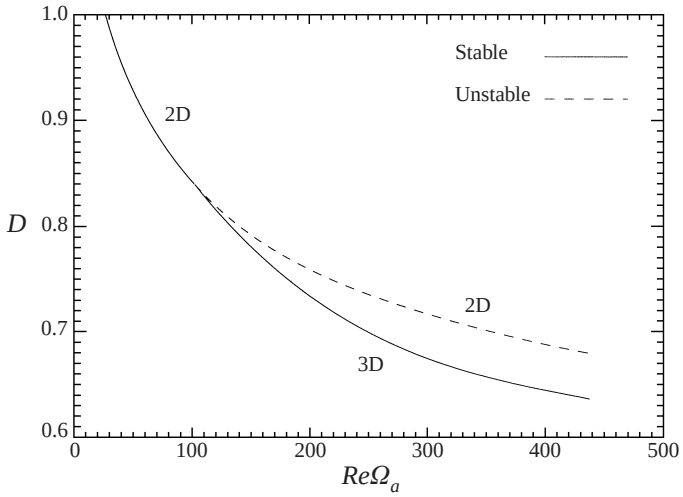

FIGURE 6. Viscous dissipation rate per unit length D (in units of $2\pi/Re$) against rotational Reynolds number $Re\Omega_a$ at $Re = 1000$ and $\alpha = 0.10695$. This clearly shows that the first and second bifurcations lead to reduced dissipation rates.

which reduces here to

$$\mathrm{D} = \frac{2\pi}{Re}\left[1 + \frac{\alpha}{\pi^2}\int_0^1\int_0^{2\pi}\int_0^{2\pi/\alpha} s\tilde{w}\,\mathrm{d}s\,\mathrm{d}\phi\,\mathrm{d}z\right]. \tag{3.4}$$

Figure 6 shows that both the first (one-dimensional to two-dimensional) and second (two-dimensional to three-dimensional) bifurcations lead to solutions with reduced dissipation rates.

In summary, we have found that the secondary bifurcation in RHPF$[\Omega_a, 0]$ from two-dimensional helical waves to three-dimensional travelling waves is a supercritical Hopf bifurcation which cannot be continued back to the HPF limit of zero rotation over the range $200 \leqslant Re \leqslant 3000$. This then is in direct contrast with the situation in narrow-gap Taylor–Couette flow (Nagata 1990). The secondary bifurcation appears to select a less dissipative three-dimensional solution when the two-dimensional helical wave starts to develop a severely flattened nose in its axial mean flow profile.

3.2. *Stability of* RHPF$[0, \Omega_p]$

Here we concentrate exclusively on the two-cell flow in RHPF$[0, \Omega_p]$ which connects smoothly onto HPF as $\Omega_p \to 0$. Sharma & Nandakumar (1995) found that this solution is linearly stable to two-dimensional disturbances over the parameter settings $\Omega_p = 0.08/Ro$ and $Re = 312.5Ro$ where $0 \leqslant Ro \leqslant 20$ (their $Ek = 1/(4Re\Omega_p)$ and $Ro = 2/(Re\Omega_p^2)$). Here, given the importance for continuation purposes, we re-examine the linear stability of this two-cell flow with respect to fully three-dimensional disturbances over the range $0 < \Omega_p \leqslant 1$ and $300 \leqslant Re \leqslant 10\,000$.

The velocity expansion used to capture the two-dimensional solution was as in (3.1) but with $c_\phi = c_z = \alpha = 0$. Convergence checks and comparisons with the work of Lei & Hsu (1990) indicated that a truncation of $(N, M) = (9, 6)$ captured the two-dimensional flow well over the range $1000 \leqslant Re \leqslant 10\,000$ and $\Omega_p \leqslant 1$. The linear stability analysis, however, was a more delicate procedure and required larger

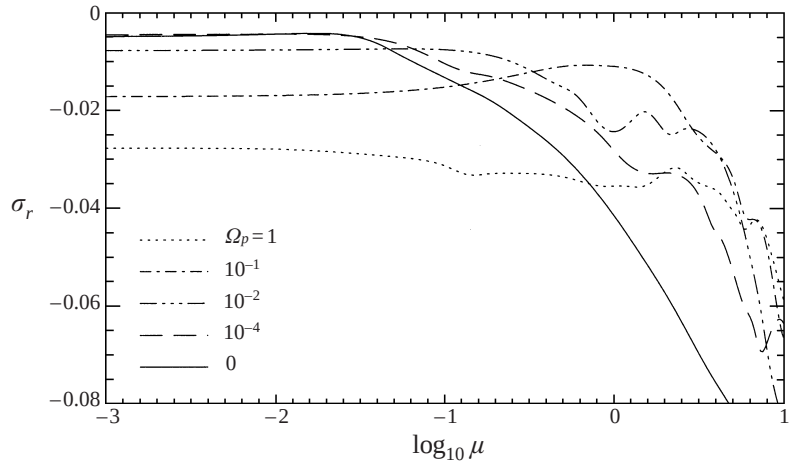

FIGURE 7. Plot of the growth rate $\sigma_r := \mathrm{Re}\,(\sigma)$ of the least stable mode in RHPF$[0, \Omega_p]$ against $\log\mu$ at $Re = 3000$ and various Ω_p values. The truncation used here is $(N, M, N_s, M_s) = (9, 6, 18, 8)$.

truncation; typically, the overall truncation used was $(N, M, N_s, M_s) = (9, 6, 18, 8)$ where (N_s, M_s) describes the truncation for the three-dimensional disturbance,

$$\begin{bmatrix} \widehat{u} \\ \widehat{v} \\ \widehat{w} \\ \widehat{p} \end{bmatrix} = \exp(\mathrm{i}\mu z + \sigma t) \sum_{n=1}^{N_s} \left\{ \sum_{m=-M_s,\, m\,\mathrm{odd}}^{M_s} \begin{bmatrix} \widehat{u}_{lmn}\Theta_{2n}(s) \\ \widehat{v}_{lmn}\Theta_{2n}(s) \\ \widehat{w}_{lmn}\Theta_{2n+1}(s) \\ \widehat{p}_{lmn}T_{2n-1}(s) \end{bmatrix} \exp(\mathrm{i}m\phi) \right.$$

$$\left. + \sum_{m=-M_s,\, m\,\mathrm{even}}^{M_s} \begin{bmatrix} \widehat{u}_{lmn}\Theta_{2n+1}(s) \\ \widehat{v}_{lmn}\Theta_{2n+1}(s) \\ \widehat{w}_{lmn}\Theta_{2n}(s) \\ \widehat{p}_{lmn}T_{2n-2}(s) \end{bmatrix} \exp(\mathrm{i}m\phi) \right\}. \qquad (3.5)$$

As before, linear instability is assured if there exists an axial wavenumber μ such that $\mathrm{Re}\,(\sigma) > 0$. Figure 7 shows that the maximum value of $\mathrm{Re}\,(\sigma)$ is always negative over $10^{-3} \leqslant \mu \leqslant 10$ for any $\Omega_p \leqslant 1$ at $Re = 3000$. Similar results at $Re = 300$, 1000 and 10 000 support the conclusion that the steady two-dimensional flow is linearly stable for $300 \leqslant Re \leqslant 10\,000$. This means that no new solution branch can be reached smoothly from the two-cell flow solution and therefore no possibility exists for continuation back to HPF from this starting flow. The four-cell flow solution which Sharma & Nandakumar (1995) found to be linearly unstable to two-dimensional disturbances, however, offers new opportunities but these have not been pursued here.

3.3. *Three-dimensional travelling waves in* RHPF$[\Omega_a, \Omega_p]$: *slow axial rotation* $\Omega_a \ll 1$

A necessary precursor to finding new three-dimensional travelling-wave solution in RHPF $[\Omega_a, \Omega_p]$ is identifying how the neutral curve in the $(Re\Omega_a, Re)$ plane of RHPF$[\Omega_a, 0]$ extends as a surface into the $(Re\Omega_a, Re\Omega_p, Re)$ space of RHPF$[\Omega_a, \Omega_p]$. This was achieved by continuing the known one-dimensional solution on the axis $\Omega_p = 0$ into its two-dimensional analogue for $\Omega_p \neq 0$ and then systematically examining linear stability to general three-dimensional disturbances. The marginal curves for $Re = 200, 500, 1000$ and 3000 are shown in figure 8. They all bend away from the

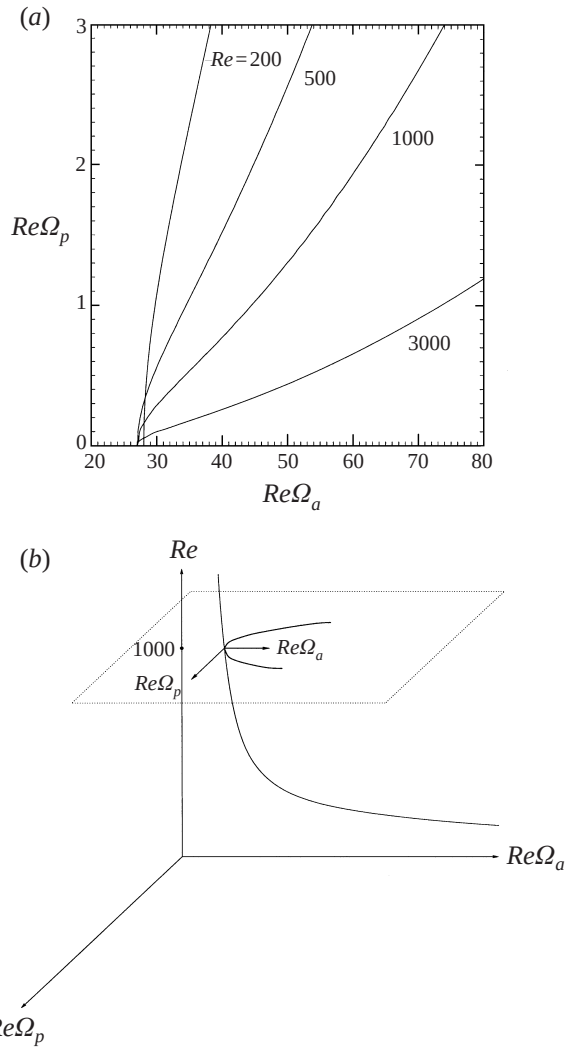

FIGURE 8. Neutral curves in RHPF$[\Omega_a, \Omega_p]$ for $Re = 200, 500, 1000$ and 3000 projected onto the plane of the two rotational Reynolds numbers in (*a*). Stable (unstable) regions are to the left (right) of the curves. Typical truncations used were $(N, M, N_s, M_s) = (7, 4, 8, 5)$ for $Re = 200$ to $(N, M, N_s, M_s) = (8, 5, 15, 7)$ for $Re = 3000$. (*b*) gives a three-dimensional perspective of how these marginal curves relate to Mackrodt's neutral curve.

$\Omega_a = 0$ axis making it clear that perpendicular rotation has a uniformly stabilizing effect in the slow axial rotation limit.

Figure 9 shows some representative three-dimensional travelling-wave solution branches emerging from the neutral curve at $Re = 1000$ for $Re\Omega_p = 2.008$ and $Re\Omega_p = 3.556$ (note the Ω_p values cannot be precisely predetermined since they are the result of a continuation procedure). This now primary bifurcation remains supercritical for $\Omega_p \neq 0$ so that three-dimensional travelling-wave solutions again can only be continued in the direction of increasing axial rotation. Plots of the energy distribution in (m, l) space emphasize that these three-dimensional solutions are really two-dimensional helical waves slightly three-dimensionalized by the small perpendicular rotation present.

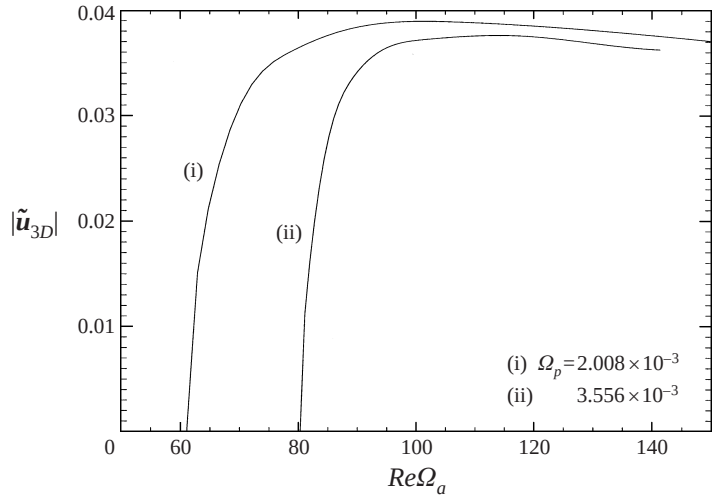

FIGURE 9. Supercritical bifurcating branches of three-dimensional solutions which emerge at two different points, $Re\Omega_p = 2.008$ ($\mu = 0.1011$) and $Re\Omega_p = 3.556$ ($\mu = 0.0867$), on the marginal stability curve for $Re = 1000$ in RHPF$[\Omega_a, \Omega_p]$. $\tilde{\boldsymbol{u}}_{3D}$ represents the three-dimensional component of the flow.

The azimuthal stress on the pipe walls is no longer vanishing in RHPF$[\Omega_a, \Omega_p]$ because the axial angular momentum of the flow (due to Ω_a) is rotating in space (due to Ω_p). The torque necessary to achieve this must come from the azimuthal shear stress which then provides a second descriptor of the flow solution along with the dissipation. Figure 10 shows that the three-dimensional solution corresponds to both less azimuthal stress and dissipation per unit length than the coexisting but unstable two-dimensional solution. This then reiterates the observation made in § 3.1.

An energy stability analysis for RHPF$[\Omega_a, \Omega_p]$ adds further support to the conclusion that Ω_p is a stabilizing influence. The application of energy stability analysis (Serrin 1959; Joseph 1976) here is somewhat non-standard because the base two-dimensional flow for $\Omega_p \neq 0$, $\boldsymbol{U}$, depends non-trivially on Re. This means that the normal expression for Re_e,

$$\frac{1}{Re_e} := \max_{\substack{\boldsymbol{u} \\ \nabla \cdot \boldsymbol{u} = 0, \boldsymbol{u} = \boldsymbol{0}|_{\partial V}}} \left\{ \frac{-\iiint \boldsymbol{u} \cdot \nabla \boldsymbol{U} \cdot \boldsymbol{u} \, \mathrm{d}\boldsymbol{x}}{\iiint |\nabla \boldsymbol{u}|^2 \, \mathrm{d}\boldsymbol{x}} \right\}, \tag{3.6}$$

may not be unique. In practice, however, this merely means selecting the global maximum or lowest value for Re_e since monotonic exponential decay is still only assured for $Re < Re_e$. The difference here is that there may be values of $Re > Re_e$ which are also absolutely stable, although this seems unlikely. For $\Omega_p = 0$, it is well known that Re_e does not depend on Ω_a because the Coriolis force is skew-symmetric and therefore does not contribute to the energy balance. This means that the critical Re for linear instability in RHPF$[\Omega_a, 0]$ can vary from ∞ at $\Omega_a < 0.027/Re$ down to 82.88 (Pedley 1969) as $\Omega_a \to \infty$, whereas Re_e is always the strictly lower bounding 81.49. The introduction of Ω_p is found to both increase Re_e slightly, for example $Re_e \approx 90$ when $\Omega_p = 0.03$, and also introduce a weak Ω_a-dependence in Re_e.

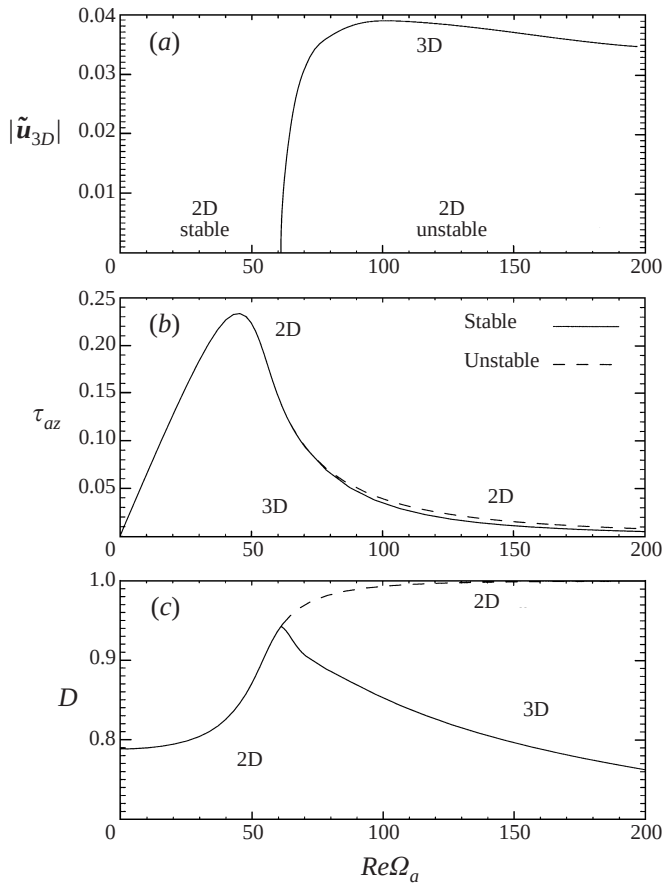

FIGURE 10. Plots of the (*a*) extended bifurcating branch, (*b*) azimuthal shear stress, and (*c*) viscous dissipation rate, all against rotational Reynolds number $Re\Omega_a$ at $Re\Omega_p = 2.008$ and $Re = 1000$. Truncation levels are $(N, M) = (9, 6)$ for the two-dimensional solutions and $(N, M, L) = (9, 6, 6)$ for the three-dimensional solutions where $\mu = 0.1011$.

3.4. *Three-dimensional travelling waves in* RHPF$[\Omega_a, \Omega_p]$*: fast axial rotation* $\Omega_a \gg 1$

It has been shown relatively recently that a rapidly rotating, fluid-filled pipe subjected to a small precession can be linearly unstable (Mahalov 1993; Kerswell 1993). This means that the neutral surface for RHPF$[\Omega_a, \Omega_p]$ cuts the (Ω_p, Ω_a)-plane in (Ω_a, Ω_p, Re) space ($Re = 0$ corresponds to a vanishing axial pressure gradient). The intersection of the neutral surface with the (Ω_a, Re)-plane is already known through Mackrodt's (1976) work and § 3.2 presents evidence that there is no intersection with the (Ω_p, Re)-plane for the generic two-cell flow. The purpose of this subsection is to map out this (Ω_p, Ω_a)-neutral curve, to explore the three-dimensional solutions which branch off from it and then to investigate if and how the neutral surface connects this curve with Mackrodt's curve.

Since flows with no applied axial pressure gradient are to be considered, a new non-dimensionalization must be temporarily adopted where the velocity scale is taken as $\Omega_a^* s_0$ rather than U. With this adjustment, the momentum equation in the precessing

frame is now written as

$$\frac{\partial \boldsymbol{v}}{\partial \tau} + 2\Omega\hat{\boldsymbol{x}}\times\boldsymbol{v} + \boldsymbol{v}\cdot\nabla\boldsymbol{v} + \nabla p = E\nabla^2\boldsymbol{v}, \tag{3.7}$$

with boundary condition $\boldsymbol{v} = \widehat{\boldsymbol{\phi}}$ at $s = 1$ (p is a modified pressure), where

$$\Omega = \frac{\Omega_p^*}{\Omega_a^*}, \quad E = \frac{\nu}{\Omega_a^* s_0^2}, \quad \epsilon = \frac{U}{\Omega_a^* s_0}, \quad \boldsymbol{v} = \frac{\boldsymbol{u}^*}{\Omega_a^* s_0}. \tag{3.8}$$

In the absence of precession, $\Omega = 0$, the basic flow is now $\boldsymbol{V} = \epsilon(1 - s^2)\widehat{\boldsymbol{z}} + s\widehat{\boldsymbol{\phi}}$ where the implication is that $0 \leqslant \epsilon \ll 1$ – the rapid rotation limit – and the conversions to the previous non-dimensional parameters and velocity are as follows

$$E = \frac{1}{Re\Omega_a}, \quad \boldsymbol{v} = \epsilon\boldsymbol{u}, \quad \tau = \frac{t}{\epsilon}, \quad \Omega = \frac{\Omega_p}{\Omega_a}, \quad \epsilon = \frac{1}{\Omega_a}. \tag{3.9}$$

For $\Omega \ll 1$ and in the absence of an applied pressure gradient ($\epsilon = 0$), the forced basic state can be expressed as the interior solution

$$\boldsymbol{V} = s\widehat{\boldsymbol{\phi}} - 2\Omega s \sin\phi\widehat{\boldsymbol{z}} + O(\Omega^2, \Omega E^{1/2}) \tag{3.10}$$

together with an $O(\Omega)$ Ekman-boundary-layer correction at $1 - s = O(E^{1/2})$. In the rapidly rotating limit $E \ll 1$, the precessional instability (Mahalov 1993; Kerswell 1993) can be understood as the resonant coupling of two normal modes of the system – inertial waves – by the interior basic solution. To illustrate this, take $E = 0$ temporarily and consider the linearized momentum equation for a small disturbance $\widehat{\boldsymbol{v}}$ upon the basic state (3.10),

$$\mathscr{L}_0\widehat{\boldsymbol{v}} := \left(\frac{\partial}{\partial t} + \frac{\partial}{\partial \phi}\right)\widehat{\boldsymbol{v}} + \widehat{\boldsymbol{z}}\times\widehat{\boldsymbol{v}} + \nabla p = \Omega(\mathrm{e}^{\mathrm{i}\phi}\mathscr{L}_1 + \mathrm{e}^{-\mathrm{i}\phi}\mathscr{L}_1^*)\widehat{\boldsymbol{v}} + O(\Omega^2) \tag{3.11}$$

where

$$\mathscr{L}_1\widehat{\boldsymbol{v}} := \begin{bmatrix} -\mathrm{i} \\ 1 \\ 0 \end{bmatrix}\widehat{w} - \mathrm{i}s\frac{\partial\widehat{\boldsymbol{v}}}{\partial z}. \tag{3.12}$$

The problem for $\Omega = 0$ is just the well-known inertial wave problem for an infinite cylinder (Greenspan 1968) which has solutions of form

$$\boldsymbol{u} = \begin{bmatrix} u \\ v \\ w \end{bmatrix} = \frac{\exp(\mathrm{i}(m\phi + \alpha z + \lambda t)}{2(4 - (\lambda + m)^2)} \times \begin{bmatrix} \mathrm{i}\{(\lambda + m + 2)J_{m-1}(ks) - (\lambda + m - 2)J_{m+1}(ks)\} \\ -\{(\lambda + m + 2)J_{m-1}(ks) + (\lambda + m - 2)J_{m+1}(ks)\} \\ 2(\lambda + m)k/\alpha J_m(ks) \end{bmatrix} \tag{3.13}$$

$$p = -\frac{1}{k}J_m(ks)\exp(\mathrm{i}(m\phi + \alpha z + \lambda t), \tag{3.14}$$

where

$$\lambda + m = \frac{\pm 2}{\sqrt{1 + k^2/\alpha^2}} \tag{3.15}$$

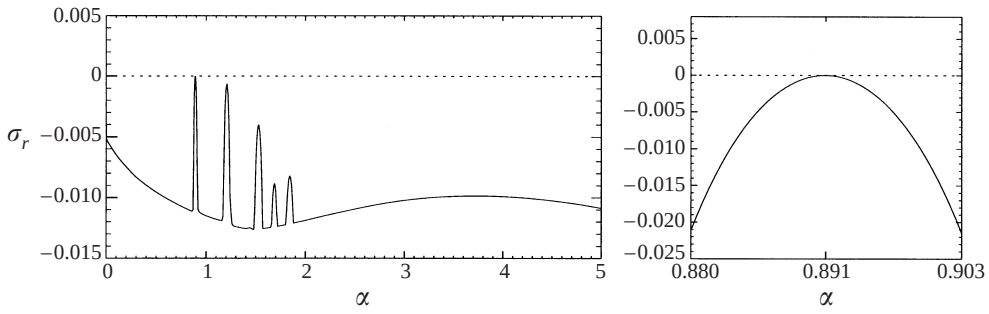

FIGURE 11. A plot of the growth rate σ_r against axial wavenumber α at $E = 2.5 \times 10^{-4}$ for linear disturbances on the precessional basic state at $\Omega = 0.0208$. This confirms that the Mahalov's instability at $\alpha \approx 0.878$ does define the neutral point (actually $\alpha_{crit} = 0.8914$).

and k is a solution indexed by n such that $0 < k_{n=1} < k_{n=2} \ldots$, of

$$s\frac{\mathrm{d}}{\mathrm{d}s}J_m(ks) + \frac{2m}{\lambda + m}J_m(ks) = 0|_{s=1}. \tag{3.16}$$

When $0 < \Omega \ll 1$, the right-hand side of (3.11) can be viewed as a small coupling term between these waves. The underlying precessional state given by (3.10) is essentially a wave of amplitude Ω with axial wavenumber 0, azimuthal wavenumber 1 and frequency 0 (in this frame). The coupling term can therefore link inertial waves whose frequencies and axial wavenumbers are equal but whose azimuthal wavenumbers differ by 1 (familiar triad resonance conditions) to produce resonant growth of the two inertial waves. To show this, consider the following expansion of the disturbance field

$$\widehat{\boldsymbol{v}} = A(T)\boldsymbol{v}_A(\boldsymbol{x}, \tau) + B(T)\boldsymbol{v}_B(\boldsymbol{x}, \tau) + \Omega\tilde{\boldsymbol{v}} + O(\Omega^2), \tag{3.17}$$

where $T = \Omega\tau$ is a slow timescale so that A and B are slowly varying amplitudes. The inertial waves represented by $\boldsymbol{v}_A$ and $\boldsymbol{v}_B$ have the same frequency λ and axial wavenumber α, but different azimuthal wavenumbers m_A and m_B, respectively, where $m_B = m_A + 1$. The $O(\Omega)$ momentum equation is

$$\mathscr{L}_0\tilde{\boldsymbol{v}} = (\mathrm{e}^{\mathrm{i}\phi}\mathscr{L}_1 + \mathrm{e}^{-\mathrm{i}\phi}\mathscr{L}_1^*)(A\boldsymbol{v}_A + B\boldsymbol{v}_B) - \frac{\mathrm{d}A}{\mathrm{d}T}\boldsymbol{v}_A - \frac{\mathrm{d}B}{\mathrm{d}T}\boldsymbol{v}_B \tag{3.18}$$

which has secular terms on the right-hand side unless the following choices are made

$$\frac{\mathrm{d}A}{\mathrm{d}T} = C_1 B := \frac{\int \mathrm{e}^{-\mathrm{i}\phi}\boldsymbol{v}_A^* \cdot \mathscr{L}_1^*\boldsymbol{v}_B \,\mathrm{d}\boldsymbol{x}}{\int |\boldsymbol{v}_A|^2 \,\mathrm{d}\boldsymbol{x}}B, \quad \frac{\mathrm{d}B}{\mathrm{d}T} = C_2 A := \frac{\int \mathrm{e}^{\mathrm{i}\phi}\boldsymbol{v}_B^* \cdot \mathscr{L}_1\boldsymbol{v}_A \,\mathrm{d}\boldsymbol{x}}{\int |\boldsymbol{v}_B|^2 \,\mathrm{d}\boldsymbol{x}}A \tag{3.19}$$

where C_1 and C_2 are real constants. Exponentially growing solutions $A, B \propto e^{\sigma T}$ exist providing $\sigma^2 = C_1 C_2 > 0$. In his paper, Mahalov (1993, table 1) finds a strong (inviscid) resonance at $\alpha = 0.878$ and $m_A = 0$ where $\sqrt{C_1 C_2} = 0.549$. Given that the absolute maximum value of $\sqrt{C_1 C_2}$ is $5\sqrt{15}/32 \approx 0.605$ (Kerswell 1993) and the large-scale nature of the flow, this instability would seem a good candidate to define the precessional neutral curve for $E \to 0$. This hypothesis was found to be correct at $E = 1/4000$ by finding the basic forced precessional solution through continuation and systematically testing its linear stability over all α: see figure 11. The lowest value of $\Omega_{crit} = 0.0208$ is, however, given by a slightly different value of $\alpha = 0.8914$ owing

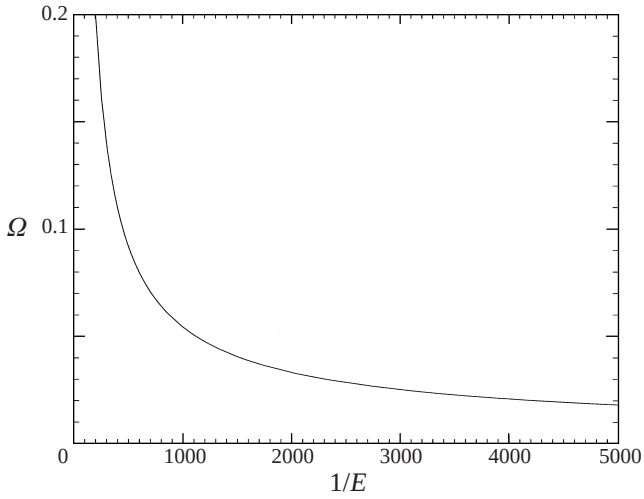

FIGURE 12. A plot of the neutral curve in the $(\Omega, 1/E)$-plane viewed from $(\Omega, 1/E, \epsilon)$-space.

to the effect of viscous frequency shifts. These are available asymptotically through standard Ekman-boundary-layer theory (see Kerswell & Barenghi 1995, equation (2.12)) and can be built into the inviscid theory given above as follows

$$\frac{\mathrm{d}A}{\mathrm{d}T} = C_1 B \mathrm{e}^{\mathrm{i}\delta T} + \frac{(\mathrm{i}\Delta\lambda_A - v_A)}{\Omega} A, \quad \frac{\mathrm{d}B}{\mathrm{d}T} = C_2 A \mathrm{e}^{-\mathrm{i}\delta T} + \frac{(\mathrm{i}\Delta\lambda_B - v_B)}{\Omega} B, \tag{3.20}$$

where $(\Delta\lambda_A + \mathrm{i}v_A)$ is, for example, the complex viscous frequency shift for inertial wave A and a small detuning between the inviscid frequencies, $\lambda_B - \lambda_A = \Omega\delta$ has also been incorporated. At $\alpha = 0.878$, (3.20) predicts $\Omega_{crit} = 0.0253$ which compares well with the numerical value found of 0.0254 (here $\lambda_A = \lambda_B = -0.446$ so $\delta = 0$, $\Delta\lambda_A = 0.449E^{1/2}$, $v_A = 0.449E^{1/2} + (k_A^2 + \alpha^2)E$, $\Delta\lambda_B = -0.576E^{1/2}$, $v_B = 0.576E^{1/2} + (k_B^2 + \alpha^2)E$ with $k_A = 3.838$ and $k_B = 3.046$). At $\alpha = 0.8914$, the inviscidly detuned system is brought into perfect resonance by the viscous frequency shifts, $\Omega\delta = \Delta\lambda_A - \Delta\lambda_B$, so that

$$\sqrt{C_1 C_2}\Omega_{crit} = \sqrt{v_A v_B} \approx [0.449E^{1/2} + (k_A^2 + \alpha^2)E]^{1/2}[0.576E^{1/2} + (k_B^2 + \alpha^2)E]^{1/2}, \tag{3.21}$$

which predicts $\Omega_{crit} = 0.021$ at $E = 1/4000$ compared to the true numerical value 0.0208.

The neutral curve in the (Ω, E)-plane (i.e. the (Ω_p, Ω_a)-plane) was traced out from $E = 1/4000$ down to $E = 1/400$: see figure 12. No mode crossing was found over this Ekman number range so that the same inertial wave pairing which defines the neutral point at $E = 1/4000$ also gives the neutral point at $E = 1/400$. At either end of this neutral line segment, three-dimensional solution branches were traced out by continuation. In both cases, the bifurcation is found to be supercritical as the branches arch towards increasing Ω. This bifurcation seems to lead to an increased dissipation (see figure 13) which is consistent with the fact that the flow is now boundary-driven rather pressure-driven. Figure 14 also shows that the three-dimensional branch can arch backwards if the starting point used ($\alpha = 0.878$ and $\Omega = 0.0254$) is some way back from the neutral curve proper ($\alpha = 0.8914$ and $\Omega_{crit} = 0.0208$), although crucially Ω_{min} is still greater than Ω_{crit}. The supercriticality of the precessional instability found here is not entirely surprising since uniformly rotating flows are well known to be

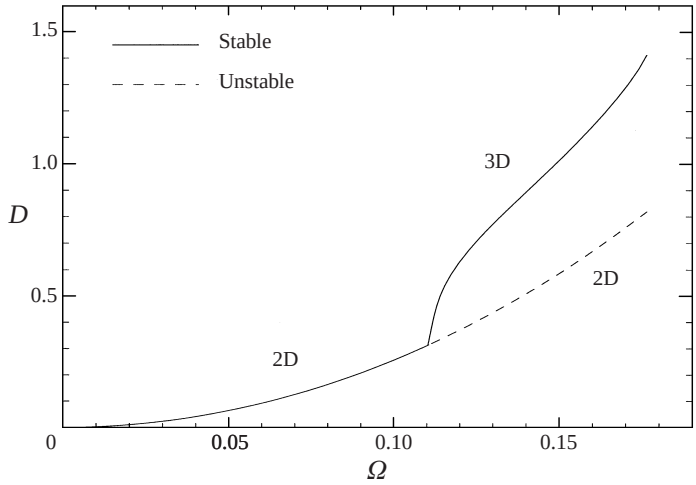

FIGURE 13. Viscous dissipation rate per unit length D (in units of $2\pi E$) against precession rate Ω at $E = 2.5 \times 10^{-3}$ and $\alpha = 0.9221$. In contrast to the pressure-driven situation, dissipation increases with bifurcation in this boundary-driven case.

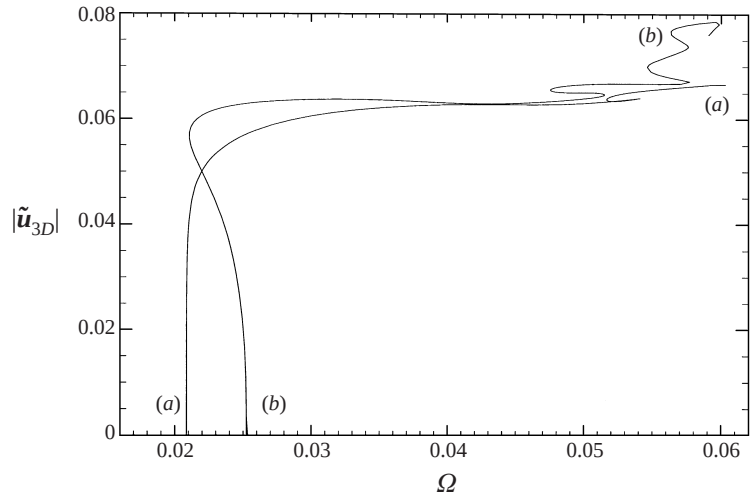

FIGURE 14. A plot of the supercritical three-dimensional solution branch – curve (a) – which emerges out of the precessional neutral curve at $\alpha = 0.8914$ and $E = 2.5 \times 10^{-4}$. Also shown is the corresponding branch – curve (b) – for $\alpha = 0.878$ which starts behind the neutral curve. Notice that Ω_{min} is still larger than Ω_{crit} for $\alpha = 0.8914$. The complicated behaviour at high Ω is the result of the finite truncation, $(N, M, L) = (12, 5, 5)$, and is undoubtedly unphysical.

absolutely stable which precludes the existence of neutral finite-amplitude travelling waves at $\Omega = 0$.

The connection between this 'precessional' neutral curve and Mackrodt's neutral curve (in the Pedley limit) is *a priori* unclear given that the respective eigenfunctions look similar in structure (Bessel-like and low azimuthal wavenumbers) except for their axial wavenumbers. At $E = 1/4000$, Mackrodt's neutral curve is given approximately by $Re_{crit} \approx 83$ and $\Omega_a = 4000/83$ so $\epsilon = 83/4000 \approx 0.02$ and $\alpha_{crit} = O(\epsilon/2) = O(0.01)$ (Pedley 1969). The precessional instability, in contrast, has $\alpha_{crit} \approx 0.9$. There seem to be three possibilities. The neutral surface could link these curves smoothly so that both

instability limits are given by essentially the same eigenfunction. Alternatively, the link could be non-smooth indicating that the two instabilities are given by different eigenfunctions. Finally, there may be no connection between the curves at all, which would arise if precession had a stabilizing influence on Pedley's fast rotation instability and vice versa.

To explore this issue, the neutral point at $(\Omega, E, \epsilon) = (0.0208, 2.5 \times 10^{-4}, 0)$ was extended to trace out a line by gradually increasing ϵ from 0. The value of Ω is found to marginally decrease to 0.02703 at $\epsilon = 0.079$ but then increase with ϵ. Crucially, α actually gets larger along this line rather than decreasing towards the required $O(0.01)$ value. Repeating this procedure but now starting at Mackrodt's neutral point also reveals a neutral curve only weakly affected by the secondary instability mechanism. Figure 15 summarizes the situation, making it clear that the neutral curves are connected but only in a non-smooth way. The inserts there show clearly that the fast-rotation instability and the precessional instability correspond to different eigenfunctions. The conclusion is then that the two instability mechanisms are different and effectively independent of each other.

4. Discussion

The main results of this paper can be conveniently brought together schematically on one figure (figure 16) using what is effectively four-dimensional space: 3 parameters (Ω_a,Ω_p,Re) + an amplitude measure A of how the flow solution differs from the underlying basic state. We now summarize these results under the original question headings listed in the introduction.

(i) *Can finite-amplitude travelling-wave solutions in* RHPF$[\Omega_a, 0]$ *be continued back to HPF?* We have found that the two-dimensional helical waves of Toplosky & Akylas (1988) become unstable to three-dimensional travelling waves in a supercritical Hopf bifurcation over the range $200 \leqslant Re \leqslant 3000$. This new branch of solutions therefore cannot be continued back to the HPF limit of zero rotation. The secondary bifurcation appears to occur when the two-dimensional helical wave starts to develop a severely flattened nose in the axial mean flow profile. A less-dissipative three-dimensional solution is then selected.

(ii) *Is the two-cell laminar flow in* RHPF$[0, \Omega_p]$ *unstable for experimentally interesting Reynolds numbers of* $O(1000)$*?* The results of a linear stability analysis carried out at $Re = 300$, 1000, 3000 and 10 000 suggest that the two-cell steady laminar flow is linearly stable for $300 \leqslant Re \leqslant 10\,000$. The neutral surface for RHPF$[\Omega_a, \Omega_p]$ in (Ω_a, Ω_p, Re) space therefore does not intersect the (Ω_p, Re)-plane (corresponding to this two-cell flow) between these Reynolds numbers.

(iii) *How does the neutral curve in the* (Ω_a, Re) *plane of* RHPF$[\Omega_a, 0]$ (Pedley 1969; Mackrodt 1976) *extend as a surface into* (Ω_a, Ω_p, Re) *space?* The neutral surface extending out of the (Ω_a, Re)-plane (Mackrodt's curve) for $\Omega_p \neq 0$ and $\Omega_a \leqslant 1$ bends away smoothly from the (Ω_p, Re)-plane. The effect of superimposing perpendicular rotation on a 'slowly' axially rotating pipe is therefore stabilizing. The primary bifurcation remains supercritical for $\Omega_p \neq 0$ leading now directly to three-dimensional travelling solutions which again are less dissipative than the underlying two-dimensional basic state. The situation is a little different for a 'rapidly' rotating pipe where $\Omega_a \gg 1$. Here, the neutral surface is essentially uninfluenced by small non-vanishing Ω_p until the threshold for precessional instability is reached. The neutral surface then turns through almost 90° to connect with the precessional neutral curve in the (Ω_p, Ω_a)-plane which has been found for the first time here. This non-smooth connection indicates

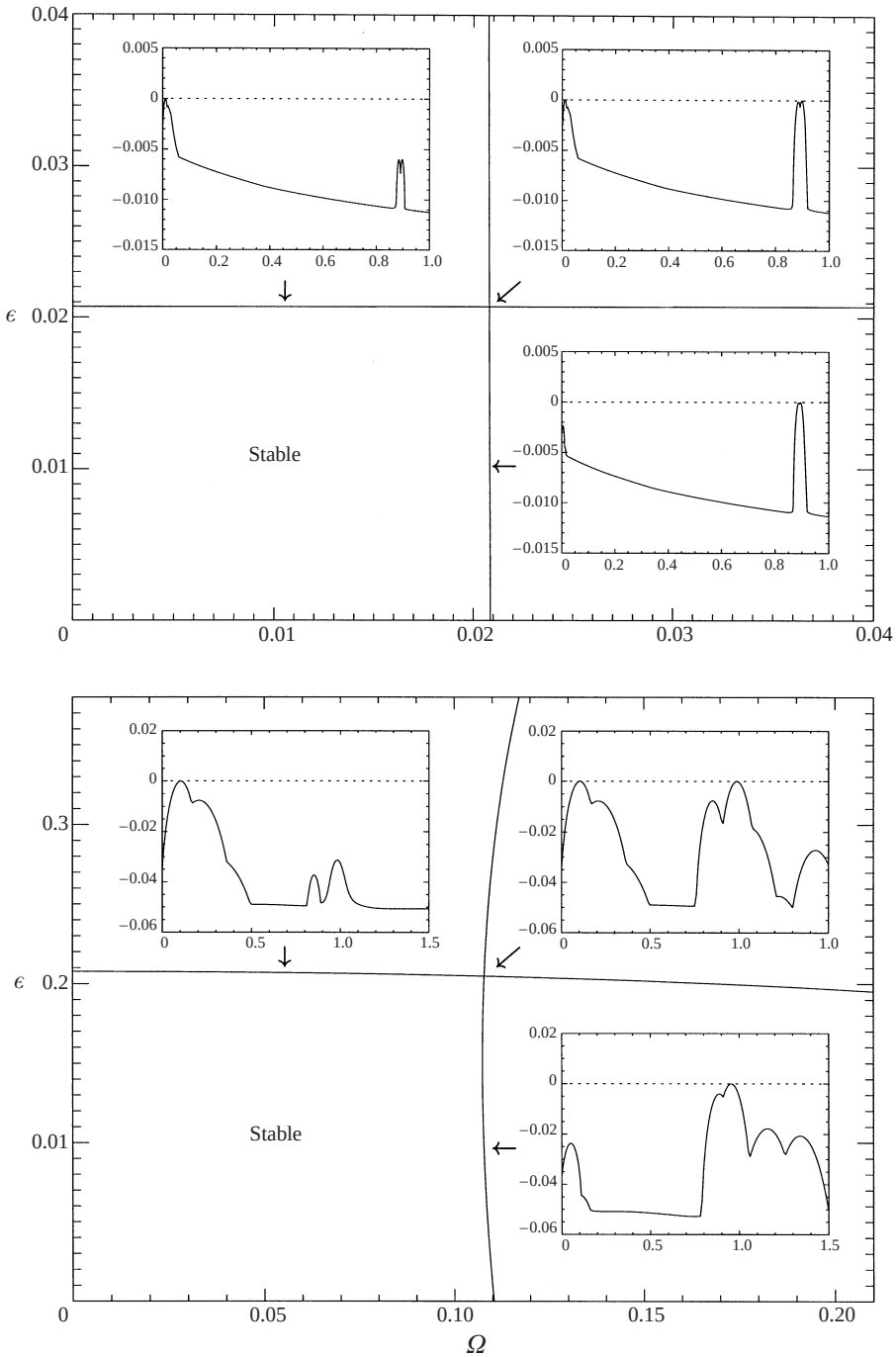

FIGURE 15. A plot of the neutral surfaces in the $(\Omega, E = 2.5 \times 10^{-4}, \epsilon)$-plane (top) and $(\Omega, E = 2.5 \times 10^{-3}, \epsilon)$-plane (bottom) to show how the Mackrodt's neutral point is connected to the precessional neutral point. The neutral surface is the union of the horizontal and vertical-looking line segments which border the stable region. The inserts show the growth rate profiles over α at certain points along this surface making it clear that the instabilities arise through different mechanisms. The Pedley instability has $\alpha \approx 0.01$ whereas the precessional instability has $\alpha \approx 0.9$.

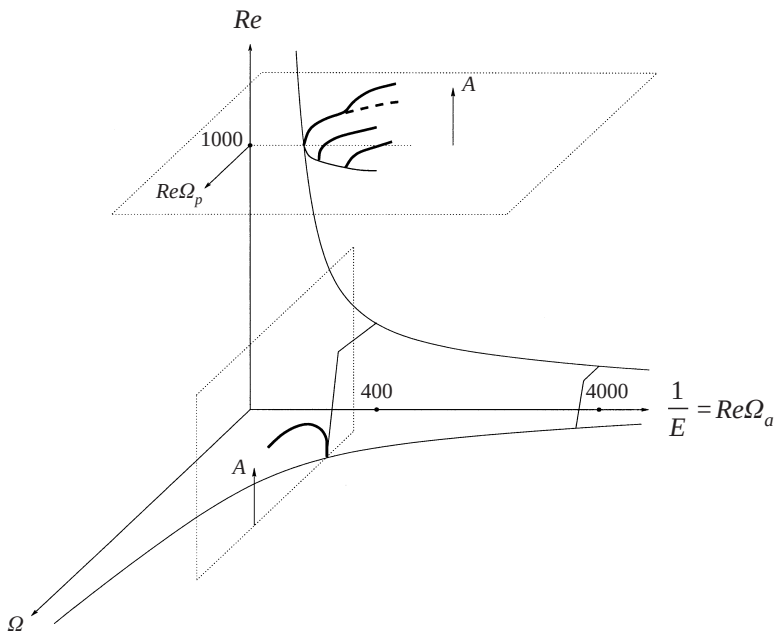

FIGURE 16. A schematic summary plot of what has been found about RHPF in this paper. The curve in the $(1/E, Re)$-plane is Mackrodt's (1976) neutral curve with $1/E \to \infty$ being the Pedley (1969) limit. The horizontal plane drawn at $Re = 1000$ with its new vertical axis A (a general measure of how the velocity solution differs from the underlying basic flow) depicts the supercritical primary bifurcation to two-dimensional helical waves and the secondary supercritical bifurcation to three-dimensional waves (§ 3.1). This neutral curve has been extended out of the plane to $\Omega_p \neq 0$ and primary bifurcation branches traced out (§ 3.3). The neutral surface has been found not to intersect the Ω-Re plane corresponding to the two-cell flow at least for $Re \leqslant 10\,000$ (§ 3.2). The curve in the $(\Omega, 1/E)$-plane is the 'precessional' neutral curve and the lines connecting the two neutral curves at $1/E = 400$ and $1/E = 4000$ indicate how the neutral surface joins them non-smoothly (§ 3.4). The vertical plane drawn at $1/E = 400$ shows the new bifurcating branch indicating that the precessional bifurcation is again supercritical (thick lines have been used to indicate finite-amplitude solutions and thin lines the neutral surface/curves).

that the two instability mechanisms at play – axial rotation on pressure-driven axial flow and precession – are essentially independent of each other. The primary precessional instability is found to be a supercritical Hopf bifurcation for $400 \leqslant 1/E \leqslant 4000$ so that again there is no possibility of continuing these solutions back to zero precession rates or ultimately to zero axial rotation rates either. Finally, the increase rather than decrease in dissipation seen at the precessional bifurcation serves to emphasize the fundamental difference between boundary-driven and pressure-driven flows.

The fact that the new three-dimensional branch of travelling-wave solutions found here in RHPF$[\Omega_a, 0]$ does not continue back to the zero rotation limit does not, of course, preclude the possibility of other subsequent bifurcating branches doing just that. However, since it is unclear how to follow what is most likely to be a tertiary Hopf bifurcation this has not been attempted here. A tertiary pitchfork bifurcation could, in principle, be traceable but the computational demands seem currently prohibitive. The situation is similar in the precessional instability limit except here the flow is already three-dimensional after the first bifurcation so that it is the second that presents difficulties.

Our general conclusion is then a reiteration and extension of Toplosky & Akylas's conclusion in 1988. Based upon continuing the primary bifurcation in RHPF$[\Omega_a, 0]$ to finite amplitude and finding it arching away from the HPF limit of zero rotation, they concluded that there was no connection between this rotational instability and the breakdown of HPF. The fact that the secondary solution branches found here also lead away from the zero rotation limit reiterates this assertion. Additionally, we have also found that their conclusion appears to hold true more generally for the larger two-parameter family of rotating pipe flows RHPF$[\Omega_a, \Omega_p]$. Here, primary flow solutions arising out of precessional instabilities also show no sign of connecting back to the non-rotating Hagen–Poiseuille limit.

We are very grateful to one of the referees for bringing the paper by Sharma & Nandakumar to our attention. D.R.B. gratefully acknowledges the support of EPSRC through a postgraduate studentship.

REFERENCES

Barua, S. N. 1954 Secondary flow in a rotating straight pipe. *Proc. R. Soc. Lond.* A **227**, 133–139.

Benton, G. S. 1956 The effect of the Earth's rotation on laminar flow in pipes. *J. Appl. Mech.* **23**, 123–127.

Carlson, D. R., Widnall, S. E. & Peeters, M. F. 1982 A flow-visualization study of transition in plane Poiseuille flow. *J. Fluid Mech.* **121**, 487–505.

Cherhabili, A. & Ehrenstein, U. 1995 Spatially localized two-dimensional finite-amplitude states in plane Couette flow. *Eur. J. Mech.* B *Fluids* **14**, 677–696.

Cherhabili, A. & Ehrenstein, U. 1997 Finite-amplitude equilibrium states in plane Couette flow. *J. Fluid Mech.* **342**, 159–177.

Clever, R. M. & Busse, F. H. 1992 Three-dimensional convection in a horizontal fluid layer subjected to a constant shear. *J. Fluid Mech.* **234**, 511–527.

Clever, R. M. & Busse, F. H. 1997 Tertiary and quaternary solutions for plane Couette flow. *J. Fluid Mech.* **344**, 137–153.

Conley, A. J. 1996 Centrifugal destabilization and restabilization of plane shear flows. *Intl J. Bifurc. Chaos* **6**, 409–413.

Darbyshire, A. G. & Mullin, T. 1995 Transition to turbulence in constant-mass-flux pipe flow. *J. Fluid Mech.* **289**, 83-114.

Dauchot, O. & Daviaud, F. 1995 Finite amplitude perturbation and spots growth mechanism in plane Couette flow. *Phys. Fluids* **7**, 335–343.

Davey, A. & Nguyen, H. P. F. 1971 Finite-amplitude stability of pipe flow. *J. Fluid Mech.* **45**, 701–720.

Daviaud, F., Hegseth, J. & Bergé, P. 1992 Subcritical transition to turbulence in plane Couette flow. *Phys. Rev. Lett.* **69**, 2511–2514.

Davies, S. J. & White, C. M. 1928 An experimental study of the flow of water in pipes of rectangular section. *Proc. R. Soc. Lond.* A **119**, 92–107.

Draad, A. A., Kuiken, G. D. C., Nieuwstadt, F. T. M 1998 Laminar–turbulent transition in pipe flow for Newtonian and non-Newtonian fluids. *J. Fluid Mech.* **377**, 267–312.

Draad, A. A. & Nieuwstadt, F. T. M. 1998 The Earth's rotation and laminar pipe flow. *J. Fluid Mech.* **361**, 297–308.

Duck, P. W. 1983 Flow through rotating straight pipes of a circular cross section. *Phys. Fluids* **26**, 614–618.

Eckhardt, B. & Mersmann, A. 1999 Transition to turbulence in a shear flow. *Phys. Rev.* E **60**, 509–517.

Ehrenstein, U. & Koch, W. 1991 Three-dimensional wavelike equilibrium states in plane Poiseuille flow. *J. Fluid Mech.* **228**, 111–148.

Greenspan, H. P. 1968 *The Theory of Rotating Fluids*. Cambridge University Press.

Herbert, T. 1977 Die Neutralfläche der ebenen Poiseuilleströmung. Habilitationsschift, Universität Stuttgart

Itō, H. & Nanbu, K. 1971 Flow in rotating straight pipes of circular cross section. *Trans. ASME* D: *J. Basic Engng* **93**, 383–394.

Joseph, D. D. & Carmi, S. 1969 Stability of Poiseuille flow in pipes, annuli and channels. *Q. Appl. Maths* **26**, 575–599.

Joseph, D. D. 1976 *Stability of Fluid Motions I and II*. Springer, Berlin.

Kerswell, R. R. 1993 The instability of precessing flow. *Geophys. Astrophys. Fluid Dyn.* **72**, 107–144.

Kerswell, R. R. & Barenghi, C. F. 1995 On the viscous decay rates of inertial waves in a rotating circular cylinder. *J. Fluid Mech.* **285**, 203–214.

Kerswell, R. R. & Davey, A. 1996 On the linear instability of elliptic pipe flow. *J. Fluid Mech.* **316**, 307–324.

Landman, M. J. 1990*a* On the generation of helical waves in circular pipe flow. *Phys. Fluids* A **2**, 738–747.

Landman, M. J. 1990*b* Time-dependent helical waves in rotating pipe flow. *J. Fluid Mech.* **221**, 289–310.

Lei, U. & Hsu, C. H. 1990 Flow through rotating straight pipes. *Phys. Fluids* A **2**, 63–75.

Lundbladh, A. & Johansson, A. V. 1991 Direct simulation of turbulent spots in plane Couette flow. *J. Fluid Mech.* **229**, 499–516.

Mackrodt, P.-A. 1976 Stability of Hagen–Poiseuille flow with superimposed rigid rotation. *J. Fluid Mech.* **73**, 153–164.

Mahalov, A. 1993 The instability of rotating fluid columns subjected to a weak external Coriolis force. *Phys. Fluids* A **5**, 891–900.

Mansour, K. 1985 Laminar flow through a slowly rotating straight pipe. *J. Fluid Mech.* **150**, 1–21.

Nagata, M. 1990 Three-dimensional finite-amplitude solutions in plane Couette flow: bifurcation from infinity. *J. Fluid Mech.* **217**, 519–527.

Nagata, M. 1997 Three-dimensional traveling-wave solutions in plane Couette flow. *Phys. Rev.* E **55**, 2023–2025.

Nagata, M. 1998 Tertiary solutions and their stability in rotating plane Couette flow. *J. Fluid Mech.* **358**, 357–378.

Orszag, S. A. 1971 Accurate solution of the Orr–Somerfeld stability equation. *J. Fluid Mech.* **50**, 689–703.

Patel, V. C. & Head, M. R. 1969 Some observations on skin friction and velocity profiles in fully developed pipe and channel flows. *J. Fluid Mech.* **38**, 181–201.

Patera, A. T. & Orszag, S. A. 1981 Finite-amplitude stability of axisymmetric pipe flow. *J. Fluid Mech.* **112**, 467–474.

Pedley, T. J. 1969 On the instability of viscous flow in a rapidly rotating pipe. *J. Fluid Mech.* **35**, 97–115.

Raszillier, H., Guiasu, I. & Durst, F. 1990 Symbolic computation of flow in a rotating pipe. *Intl J. Numer. Meth. Fluids* **11**, 267–285.

Reynolds, O. 1883 An experimental investigation of the circumstances which determine whether the motion of water shall be direct or sinuous and of the law of resistance in parallel channels. *Phil. Trans. R. Soc.* **174**, 935–982.

Rheinboldt, W. C. & Burkardt, J. V. 1983*a* A locally parameterized continuation process. *ACM Trans. Math. Software* **9**, 215–235.

Rheinboldt, W. C. & Burkardt, J. V. 1983*b* ALGORITHM 596 A program for a locally parameterized continuation process. *ACM Trans. Math. Software* **9**, 236–241.

Schmiegel, A. & Eckhardt, B. 1997 Fractal stability border in plane Couette flow. *Phys. Rev. Lett.* **79**, 5250–5253.

Serrin, J. 1959 On the stability of viscous fluid motions. *Arch. Rat. Mech. Anal.* **3**, 1–13.

Sharma, R. K. & Nandakumar, K. 1995 Multiple, two-dimensional solutions in a rotating straight pipe. *Phys. Fluids* **7**, 1568–1575.

Smith, F. T. & Bodonyi, R. J. 1982 Amplitude-dependent neutral modes in the Hagen–Poiseuille flow through a circular pipe. *Proc. R. Soc. Lond.* A **384**, 463–489.

Tillmark, N. and Alfredsson, P. H. 1992 Experiments on transition in plane Couette flow. *J. Fluid Mech.* **235**, 89–102.

Toplosky, N. & Akylas, T. R. 1988 Nonlinear spiral waves in rotating pipe flow. *J. Fluid Mech.* **190**, 39–54.

Yang, Z. & Leibovich, S. 1991 Nonlinear dynamics near the stability margin in rotating pipe flow. *J. Fluid Mech.* **233**, 329–347.

Zahn, J.-P., Toomre, J., Spiegel, E. A. & Gough, D. O. 1974 Nonlinear cellular motions in Poiseuille channel flow. *J. Fluid Mech.* **64**, 319–345.